Article

Excellent high-temperature dielectric energy storage performance in bilayer nanocomposites with high-entropy ferroelectric oxide fillers

Xuan Zhao[1,2], Lei Zhang[1,2], Zhenhao Fan [3], Yuyan Huang[1,2], Yongming Hu[1] ✉, Meng Shen [1], Zhao Wang[1], Yunbin He [1,2] ✉, Dawei Wang [3] ✉ & Qingfeng Zhang [1,2] ✉

The low dielectric constant, limited breakdown strength, and large polarization hysteresis and conduction loss constrain discharged energy density and efficiency of polymer-based dielectric capacitors at elevated temperatures. To address these challenges, the [0.8(Na$_{0.2}$Bi$_{0.2}$Ba$_{0.2}$Sr$_{0.20}$Ca$_{0.2}$)TiO$_3$-0.2NaNbO$_3$]@Al$_2$O$_3$ high-entropy ferroelectric nanoparticles/polyetherimide-AlN/polyetherimide-triptycene bilayer nanocomposites are designed. The bilayer nanocomposites capitalize on advantages of high-entropy ferroelectric fillers, which contribute to the high dielectric constant and minimal hysteresis at high temperatures. Additionally, they also benefit from high thermal conductivity of AlN, enhanced rigidity and charge carrier traps in polyetherimide-triptycene, and suppressed carrier transport at the bilayer film interfaces. Consequently, the bilayer nanocomposites exhibit significantly improved dielectric constant and breakdown strength, and marked reduction in conduction loss at elevated temperatures. Remarkably, a record-high discharged energy density of 12.35 J cm^{-3} is achieved in the optimized bilayer nanocomposites at 150 °C, accompanied by a large efficiency of 90.25% under an electric field of 6341 kV cm^{-1}.

Dielectric capacitors are key components of advanced electronic and electrical power systems due to their higher power density (~10^7 W kg^{-1}), faster discharge rate (<100 ns), and longer cycle life (>10^6 cycles) compared to other energy storage devices, such as batteries, fuel cells, and supercapacitors[1–3]. In current dielectrics used for capacitors, polymer dielectrics exhibit advantages in flexibility, scalability, and breakdown strength (E_b), making them ideal for scalable high-energy-density capacitors[1,2,4,5]. However, a major limitation of polymer dielectrics is their poor thermal stability, which hinders them from meeting the ever-increasing demand for high-temperature (≥150 °C)

capacitors in hybrid electric vehicles, underground oil and gas explorations, high power weapon systems, etc[2,5]. Typically, the commercial polymer dielectrics, represented by biaxially oriented polypropylene (BOPP), can only work reliably below 105 °C[2]. Hence, high-performance polymer dielectrics capable of stable operation at elevated temperatures are highly desirable.

The glass transition temperature (T_g) is a critical parameter for polymers in high-temperature capacitor applications, because above T_g, polymer chains would lose their stiffness, leading to large variations in dielectric constant (ε_r) and loss (tanδ)[5,6]. Thus, high-T_g polymer, i.e.,

[1]Hubei Key Laboratory of Micro-Nanoelectronic Materials and Devices, Hubei University, Wuhan, China. [2]School of Materials Science&Engineering, Hubei University, Wuhan, China. [3]Precision Acousto-Optic Instrument Institute, School of Instrumentation Science and Engineering, Harbin Institute of Technology, Harbin, China. ✉e-mail: huym@hubu.edu.cn; ybhe@hubu.edu.cn; wangdawei102@gmail.com; zhangqingfeng@hubu.edu.cn

polyimide (PI, $T_g \approx 360\,°C$), polyetherimide (PEI, $T_g \approx 217\,°C$), and polycarbonate (PC, $T_g \approx 150\,°C$) have emerged as promising candidates for high-temperature dielectric capacitors[7]. However, good thermal stability alone does not guarantee superior capacitive performance. This is because the conduction current exponentially increases at high temperatures and large electric fields, which results in large conduction loss, and thus sharply reduced discharged energy density (U_e) and charge-discharge efficiency (η) even at the temperature below T_g of polymers[6,7]. For example, the U_e and η of PI drop drastically from 1.53 J cm^{-3} and 95.2 % at room temperatures to 0.6 J cm^{-3} and 21.8% at 150 °C, respectively[6,8]. Additionally, these polymers typically exhibit low ε_r (<5), further limiting U_e enhancement[6]. To address these challenges, inorganic nanofillers with high ε_r and wide bandgap (E_g), i.e., ZrO$_2$ ($\varepsilon_r \approx 25$, $E_g \approx 5.8$ eV), GaF$_2$ ($\varepsilon_r \approx 10$, $E_g \approx 12.1$ eV), Al$_2$O$_3$ ($\varepsilon_r \approx 9.5$, $E_g \approx 8.6$ eV), and HfO$_2$ ($\varepsilon_r \approx 25$, $E_g \approx 5.8$ eV) have been incorporated into polymer matrix[1,8–11]. These fillers increase ε_r of the polymer composites, and effectively impede charge injection and transport by creating deeper trap depth and adding more trap sites for charge carriers[1,8–11]. Nevertheless, as ε_r of these fillers is only slightly higher than polymer matrix, high volume fraction of fillers (>10 vol%) is needed for appreciable improvement of the U_e[9,12]. This results in severe filler aggregation, increased interfacial defects (such as impurities and voids), and degraded flexibility, uniformity, and processability of polymers, and the U_e is still below 8.5 J cm^{-3} (at $\eta \geq 90\%$) at 150 °C[9,12]. Alternatively, high-ε_r ferroelectric fillers (e.g., BaTiO$_3$) can boost U_e but drastically reduce η at high temperatures due to large remnant electric displacement (D_r), and high polarization and conduction loss of ferroelectric fillers at high temperatures[13,14]. For instance, the η of the BaTiO$_3$-PEI nanocomposites is only ~60% at 140 °C[13]. Thus, there is an urgent need for optimized fillers that simultaneously enhance U_e and η in high-temperature polymer composites.

Recently, lead-free high-entropy dielectric energy storage ceramics with the configuration entropy (ΔS_{config}) $\geq 1.61\,R$ (R being the ideal gas constant) have garnered significant attention attributed to their high ε_r, low tanδ, large maximum electric displacement (D_{max}), near-zero D_r, tiny electrical hysteresis, and enhanced E_b across wide temperature range (Fig. 1 and Supplementary Fig. 1)[15–17]. Encouragingly, these characteristics make high-entropy ferroelectrics exceptionally promising as fillers for developing high-temperature polymer composite capacitors. In this work, we present an innovative strategy to fabricate polymer nanocomposites with excellent high-temperature capacitive performances by incorporating core-shell structured [0.8(Na$_{0.2}$Bi$_{0.2}$Ba$_{0.2}$Sr$_{0.20}$Ca$_{0.2}$)TiO$_3$-0.2NaNbO$_3$]@Al$_2$O$_3$ (NBBSCT-NN@A) high- entropy ferroelectric nanoparticles (NPs) into PEI matrix, and constructing bilayer structure with AlN/PEI-triptycene (TE) layer, as schematically illustrated in Fig. 1. The NBBSCT-NN high-entropy ferroelectrics possess high D_{max}, low D_r, and extremely slim electric displacement-electric field (D-E) loops at 150 °C, and the Al$_2$O$_3$ shell layer provides a wide band gap (≈8.6 eV), high thermal conductivity (>30 W m^{-1} K^{-1}) and close ε_r relative to that (≈3) of pristine PEI[9,10,18]. Thus, the incorporation of NBBSCT-NN@A nanofillers into PEI enables polymer nanocomposites to achieve both high U_e and η at elevated temperatures even at remarkably low filler loadings. Compared to pristine PEI, PEI-TE polymers with dense physical crosslinking networks possess better rigidity and more traps for charge carriers, beneficial for inhibiting electromechanical and electrical breakdown[19]. Furthermore, the incorporated AlN NPs provide exceptional thermal conductivity (319 W m^{-1} K^{-1}), significantly improving heat dissipation within the composite[20]. Also, giant ε_r and electrical conductivity differences between AlN/PEI-TE and NBBSCT-NN@A/PEI layers enhance interfacial polarization while effectively suppressing electrical tree propagation, in favor of increasing the D_{max} and E_b. Consequently, encouragingly, at 150 °C, an ultrahigh U_e of 12.35 J cm^{-3}, which is the record-high value in polymer and polymer composites, and a large η of 90.25% at 6341 kV cm^{-1} are achieved in the bilayer-structured polymer

nanocomposite with ultralow loading of NBBSCT-NN@A (0.4 wt%) and AlN (0.4 wt%) fillers. Furthermore, the optimized bilayer nanocomposite displays an ultrahigh power density of 31.7 MW cm^{-3}, and an ultrafast discharge rate of 16 ns at 2000 kV cm^{-1}.

Results and discussion
Microstructure and dielectric energy storage properties of high-entropy ferroelectrics and high-entropy ferroelectric NPs/PEI nanocomposites

Figure 2a presents transmission electron microscopy (TEM) and energy dispersive spectroscopy (EDS) elemental mapping images of NBBSCT-NN@A NPs. The Ba, Bi, Na, Ca, Nb, Ti, and Sr element signals exhibit strong intensity in the core layer of the particles and disappear sharply in the shell layer, but the Al element signal exists in the whole core and shell layers. This confirms the successful formation of a continuous Al$_2$O$_3$ coating layer surrounding the NBBSCT-NN core. Besides, the NBBSCT-NN NPs display an average diameter of 158 nm with a uniform 16 nm-thick Al$_2$O$_3$ coating layer. Figure 2b presents X-ray photoelectron spectroscopy (XPS) full spectra of the NBBSCT-NN and NBBSCT-NN@A NPs. Ba, Bi, Na, Ca, Nb, Ti, and Sr peaks are clearly observed in these two kinds of NPs, and an extra Al 2p peak is found in the spectra of NBBSCT-NN@A, which can be more clearly seen in the high-resolution XPS spectra of Al 2p core levels of NBBSCT-NN@A NPs (the inset of Fig. 2b). This further indicates the successful fabrication of NBBSCT-NN@A NPs. X-ray diffraction (XRD) patterns of NBBSCT-NN and NBBSCT-NN@A NPs (Supplementary Fig. 2) reveal identical peak positions for both samples, confirming the amorphous nature of the Al$_2$O$_3$ shell layer. Figure 2c and the inset exhibit frequency and temperature dependence of the ε_r and tanδ of NBBSCT-NN ceramics. With increasing measuring frequencies from 1 to 10^6 Hz, the ε_r decreases slightly attributed to suppressed dipolar (orientational) polarization[6], but it is still as high as 1495, and the maximum tanδ is only 1.42% even at 150 °C. In addition, during 25–150 °C, the ε_r at 1 kHz is higher than 1600 with variations less than 1%, and the tanδ is always smaller than 1.36%. Figure 2d and e present unipolar D-E loops and capacitive properties of the NBBSCT-NN ceramic over a temperature range of 25–150 °C, respectively. Obviously, the ceramic maintains slim and temperature-stable loops with large D_{max} (>29.5 μC cm^{-2}), low D_r (<2.7 μC cm^{-2}), and excellent η (>86.7%) with minimal variation (<4.3%). Superior dielectric and energy storage performances of NBBSCT-NN ceramics during 25–150 °C suggest that NBBSCT-NN NPs are highly promising fillers for polymer nanocomposites requiring stable high-temperature capacitive performances. Moreover, the Al$_2$O$_3$ shell further improves thermal stability, endowing NBBSCT-NN@A ceramics with dielectric and capacitive properties that match or exceed the temperature stability of NBBSCT-NN ceramics (Supplementary Fig. 3). The energy storage properties of 0.2 wt%, 0.6 wt%, and 0.8 wt% NBBSCT-NN@A/PEI nanocomposites with different Al$_2$O$_3$ contents are summarized in Supplementary Fig. 4. The nanocomposites demonstrate optimal energy storage performance when the Al$_2$O$_3$ content constitutes 2% of the NBBSCT-NN weight. To systematically investigate the effects of NBBSCT-NN@A content on the capacitive properties of NBBSCT-NN@A/PEI nanocomposites, the weight ratio of Al$_2$O$_3$ to NBBSCT-NN is fixed at 2% in subsequent studies. Figure 2f reveals XRD patterns of NBBSCT-NN@A/PEI nanocomposites with various amount of fillers. Increasing filler content enhances the characteristic peak intensity of NBBSCT-NN NPs at ~32°, which demonstrates that the crystal structure of NBBSCT-NN fillers in the nanocomposites cannot be changed. In addition, field-emission scanning electron microscopy (FE-SEM) and EDS elemental mapping images (Fig. 2g, and Supplementary Figs. 5, 6) confirm that, for all nanocomposites, the NPs are homogeneously distributed in the PEI matrix without observable aggregation. The dielectric properties of NBBSCT-NN@A/PEI nanocomposites (Fig. 2h) at 150 °C exhibit that raising filler content enhances significantly the ε_r of the nanocomposites because of far
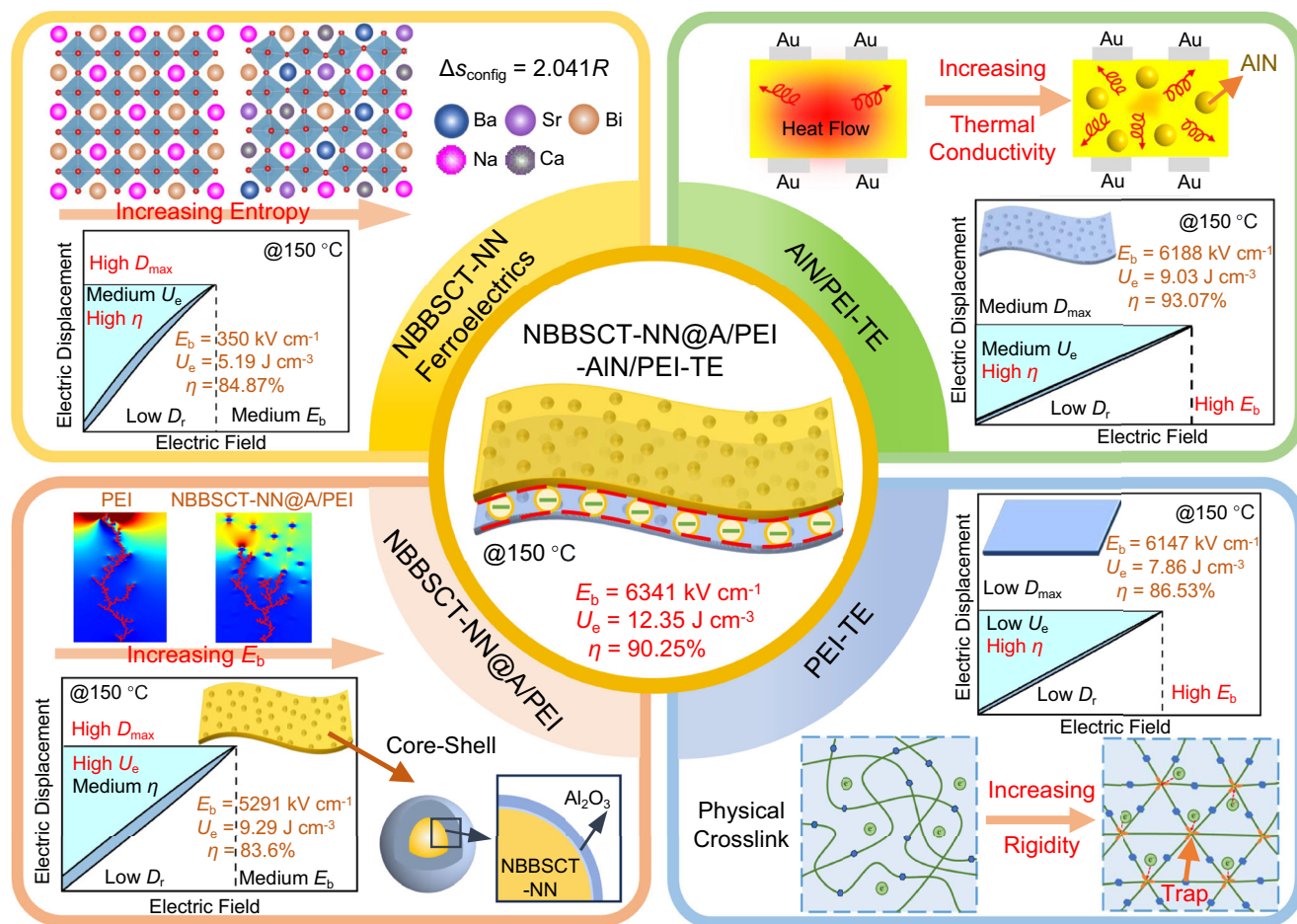
Fig. 1 | Design idea. Schematic illustration of achieving excellent high-temperature dielectric energy storage properties in high-entropy ferroelectric NPs filled bilayer-structured nanocomposites.

higher ε_r of NBBSCT-NN compared to that of the PEI matrix, as well as enhanced interfacial polarization between the polymer and NPs[6,21]. Moreover, The ε_r exhibits a mild frequency-dependent decrease, attributable to the progressive suppression of both dipolar (orientational) and interfacial polarization mechanisms at elevated frequencies[6,21]. Remarkably, all nanocomposites maintain an exceptionally low $\tan\delta$ (<1.3%) across the broad frequency range of 1 kHz-1 MHz, which originates from the intrinsically low $\tan\delta$ of NBBSCT-NN fillers. This outstanding property enables the development of high-efficiency capacitors for elevated-temperature applications. Besides, in order to confirm the repeatability of the interfacial polarization, we have measured dielectric properties of different regions in the large-area 0.8 wt% NBBSCT-NN@A/PEI nanocomposite (Supplementary Fig. 7). As observed, the ε_r at each region is nearly the same, and the $\tan\delta$ is low, indicating excellent repeatability of the interfacial polarization. This is primarily because the loading of fillers is low, allowing the NPs to be homogeneously distributed in the PEI matrix without aggregation, as evidenced by the above FE-SEM images. As shown in Supplementary Fig. 1, increased E_b is fairly effective in improving the U_e, and hence we calculate the E_b of NBBSCT-NN@A/PEI nanocomposites with various filler content at 150 °C using Weibull distribution functions[22]:

$$X_i = \ln(E_i) \tag{1}$$

$$Y_i = \ln(-\ln(1 - i/(n+1))) \tag{2}$$

where n and i represent the total number of samples and the sample serial number, respectively, while E_i is the breakdown electric field of

each sample. The shape parameter (β), derived from the slope of the linear fit between X_i and Y_i, quantifies the statistical scatter of the breakdown data. The E_b corresponds to the intersection of the fitted lines at $Y_i = 0$. As presented in Fig. 2i, the lowest β value is still as large as 16.37, indicating exceptional reliability of the E_b value, and incorporating an optimal content of NBBSCT-NN@A NPs significantly enhances the E_b of PEI nanocomposites. For example, the NBBSCT-NN@A/PEI nanocomposite achieves a maximum E_b of 5291 kV cm^{-1} at the optimal filler loading of 0.4 wt%, representing a 5.1% enhancement over pristine PEI (5035 kV cm^{-1}). However, beyond this critical concentration, the E_b declines due to increased defects at the interfaces of NBBSCT-NN@A and PEI. Figure 2j and Supplementary Fig. 8 present D-E loops, D_{max}, D_r, and D_{max}-D_r of pristine PEI and PEI nanocomposites with varying filler loading near their E_b at 150 °C. The incorporation of NBBSCT-NN@A NPs effectively slims D-E loops and enhances the D_{max}-D_r. For instance, at the optimized loading of 0.4 wt%, the D_r and D_{max}-D_r are 0.4 and 3.67 μC cm^{-2}, respectively, for NBBSCT-NN@A/PEI nanocomposites, whereas the corresponding values are 0.57 and 2.36 μC cm^{-2}, respectively, for pristine PEI. Figure 2k displays capacitive performances of NBBSCT-NN@A/PEI nanocomposites and pristine PEI at 150 °C and different electric fields, calculated from D-E loops in Supplementary Fig. 9. With improving electric field, the U_e obviously enhances, and the η slightly decreases. In addition, benefited from the concurrent improvement of E_b and D_{max}-D_r, and the decrease of D_r, the U_e and η reach the maximum value of 9.29 J cm^{-3} and 83.6%, which are more superior than 3.79 J cm^{-3} and 53.17% of pristine PEI, at 0.4 wt% filler content. Interestingly, the energy storage performances demonstrate superior temperature, frequency, and cycle stability during 25–150 °C,
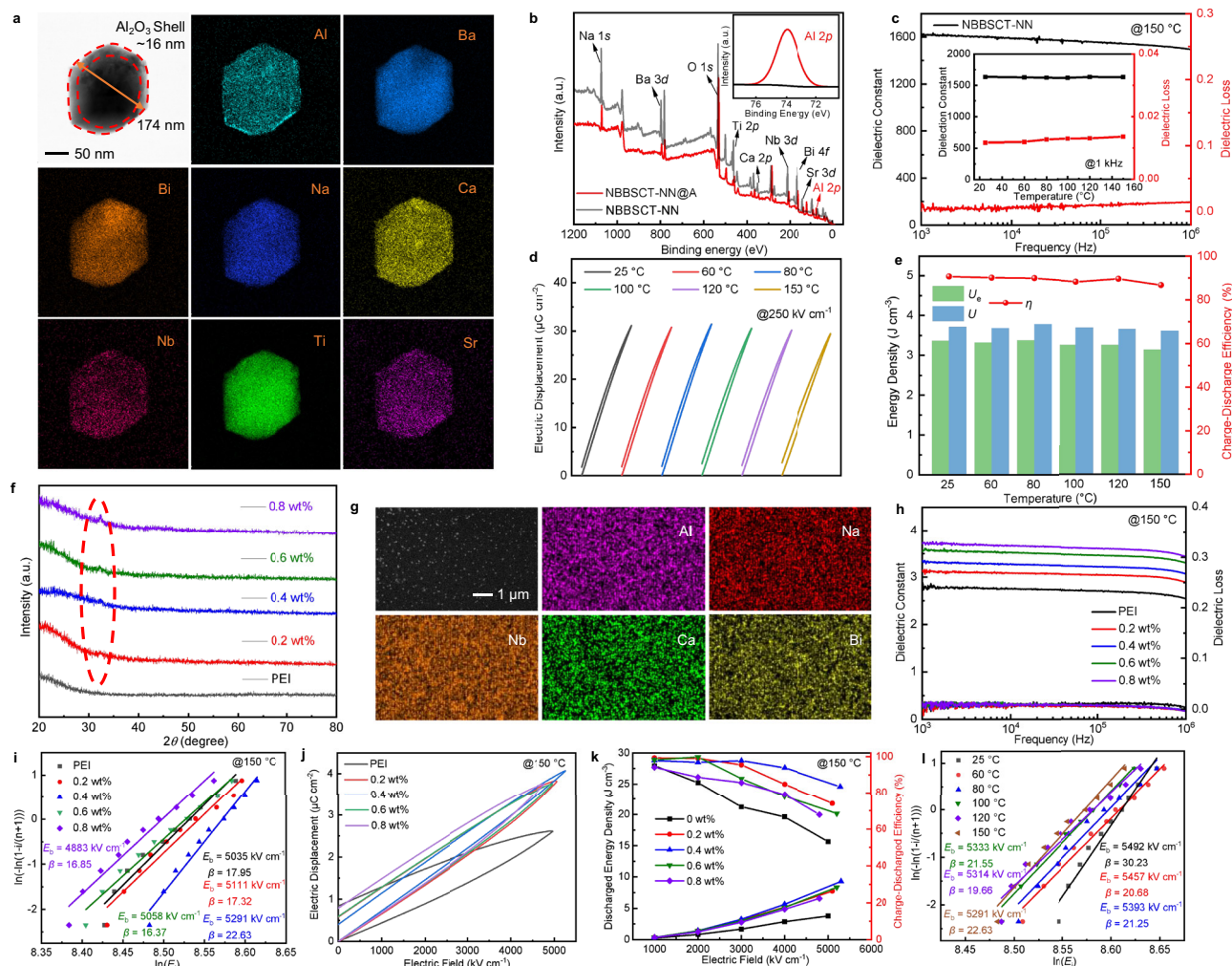
Fig. 2 | Microstructure and capacitive properties of high-entropy ferroelectrics and high-entropy ferroelectric NPs/PEI nanocomposites. a TEM and TEM-EDS elemental mapping images of NBBSCT-NN@A NPs. **b** XPS full spectra of NBBSCT-NN and NBBSCT-NN@A NPs. The inset gives high-resolution XPS spectra of Al 2p core levels of NBBSCT-NN@A NPs. **c** Frequency and temperature (the inset) dependence of the ε_r and tanδ of the NBBSCT-NN ceramic. **d** Unipolar $D\text{-}E$ loops and **e** capacitive properties of the NBBSCT-NN ceramic during 25–150 °C. **f** XRD patterns of NBBSCT-NN@A/PEI nanocomposites with various filler contents. **g** FE-SEM images of the 0.6 wt% NBBSCT-NN@A/PEI nanocomposites and EDS elemental mapping images. **h** Frequency dependence of the ε_r and tanδ, **i** Weibull distributions and E_b, **j** unipolar $D\text{-}E$ loops, and **k** electric field dependence of energy storage performances of NBBSCT-NN@A/PEI nanocomposites with different filler loadings at 150 °C. **l** Weibull distributions and E_b of NBBSCT-NN@A/PEI nanocomposites with 0.4 wt% filler contents during 25-150 °C.

100–500 Hz, and 1–10^5 cycle number, as evidenced by Fig. 2l and Supplementary Figs. 10, 11, which significantly expands the operational range of high-entropy NP/PEI nanocomposites for advanced capacitor applications.

Dielectric energy storage and charge-discharge properties of NBBSCT-NN@A/PEI-AlN/PEI-TE bilayer nanocomposites

Fourier transform infrared (FTIR) spectroscopy and XRD patterns of PEI and PEI-TE polymers (Supplementary Fig. 12a, b) reveal that with the introduction of TE, without any new chemical bonds appear, and the distances between the polymer molecular chains decrease, indicating physical crosslinking characteristics of PEI-TE polymers and enhanced rigidity. Hence, compared to pristine PEI, the PEI-TE polymers show greatly enhanced E_b (6147 kV cm^{-1}), U_e (7.86 J cm^{-3}), and η (86.53%), as illustrated in Supplementary Fig. 12c. Supplementary Fig. 13 presents microstructure of AlN/PEI-TE with varying AlN contents, and EDS elemental mapping images of the representative 0.6 wt% AlN/PEI-TE nanocomposites, confirming the uniform distribution of AlN in the PEI-TE matrix. Supplementary Fig. 14a gives Weibull distribution and E_b of AlN/PEI-TE nanocomposites with various AlN fillers

at 150 °C. The E_b initially increases with AlN content, reaching a maximum value of 6188 kV cm^{-1} at 0.4 wt% due to high thermal conductivity of AlN and enhanced charge trap density at the AlN/PEI-TE interfaces, and then decreases. In addition, with incorporating AlN fillers, the $D\text{-}E$ loops become slim, the D_{max} ($D = \varepsilon_0\varepsilon_r E$, ε_0 is the vacuum dielectric constant) improves due to higher ε_r of AlN relative to that of PEI-TE[23,24], and the $D_{max}\text{-}D_r$ enhances (Supplementary Fig. 14b–h). Thus, at 0.4 wt% filler content, the AlN/PEI-TE nanocomposite displays the highest U_e value of 9.03 J cm^{-3} accompanied by a large η of 93.07% (Supplementary Fig. 14i), and the capacitive properties remain stable across 25-150 °C (Supplementary Figs. 14–16). Furthermore, the energy storage characteristics at high temperatures exhibit good frequency and cycling stability (Supplementary Fig. 17). These results collectively confirm that AlN filler incorporation effectively enhances high-temperature capacitive properties of polymer nanocomposites.

Figure 3a and Supplementary Fig. 18a, b display the cross-section morphology of NBBSCT-NN@A/PEI-AlN/PEI-TE bilayer nanocomposites with varying thickness ratio between NBBSCT-NN@A/PEI and AlN/PEI-TE layers, which are composed of 0.4 wt% NBBSCT-NN@A/PEI and 0.4 wt% AlN/PEI-TE layers with good capacitive performances. The
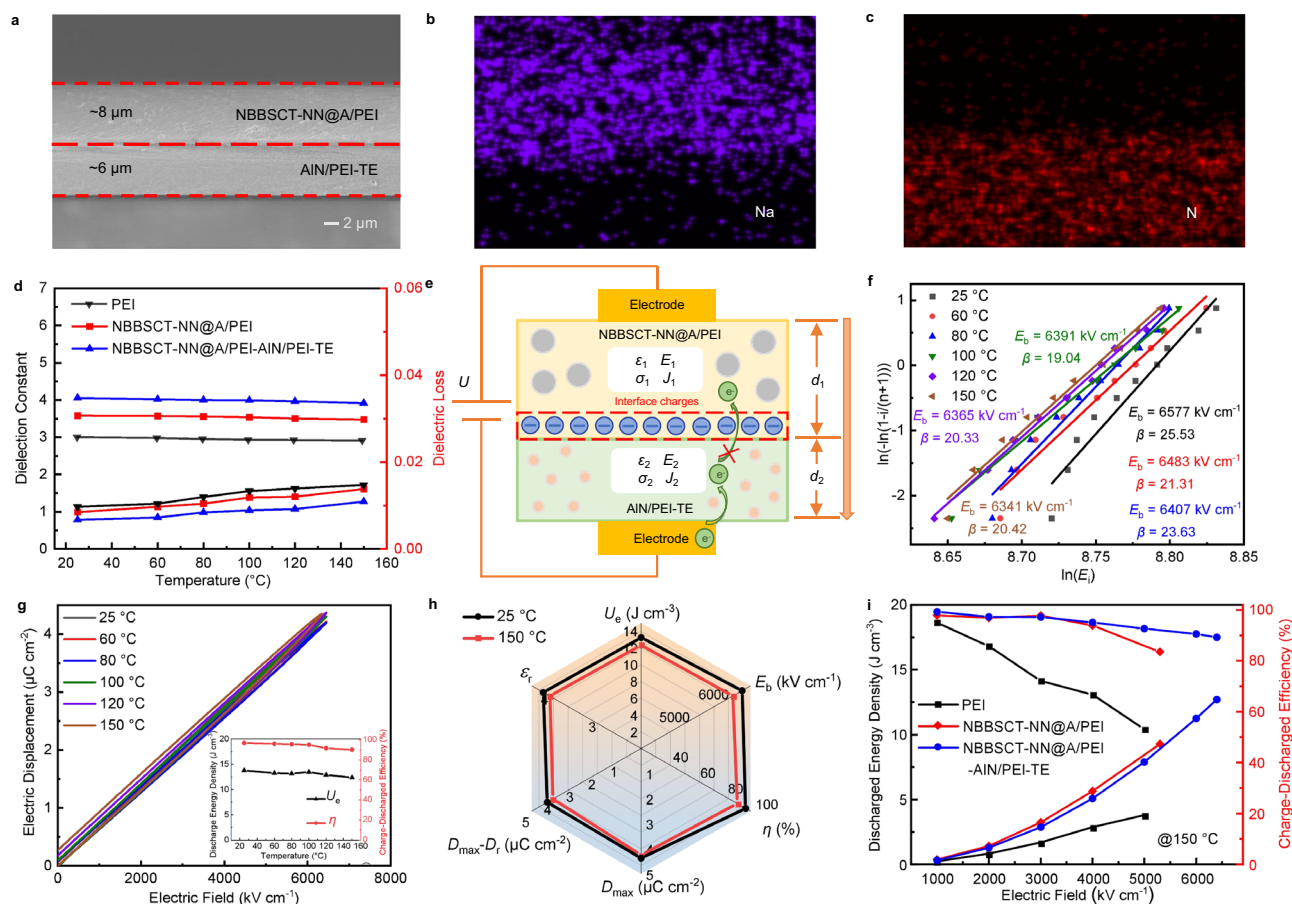
Fig. 3 | Microstructure and capacitive properties of NBBSCT-NN@A/PEI-AlN/PEI-TE bilayer nanocomposites. a The cross-section morphology, EDS elemental mapping images of **b** Na and **c** N of NBBSCT-NN@A/PEI-AlN/PEI-TE bilayer nanocomposites. **d** Temperature dependence of the ε_r and $\tan\delta$ of pristine PEI, and NBBSCT-NN@A/PEI and NBBSCT-NN@A/PEI-AlN/PEI-TE nanocomposites. **e** Dielectric model of the bilayer nanocomposites (J and δ being conduction current density and electrical conductivity, respectively). **f** Weibull distributions and E_b, and **g** unipolar D-E loops and capacitive performances (the inset) of the bilayer nanocomposites during 25–150 °C. **h** Overall capacitive properties of the bilayer nanocomposites at 25 and 150 °C. **i** Energy storage performances of pristine PEI, and NBBSCT-NN@A/PEI and NBBSCT-NN@A/PEI-AlN/PEI-TE nanocomposites at various electric fields.

thicknesses of the NBBSCT-NN@A/PEI layers are about 10 μm, 8 μm, and 6 μm, respectively, and the thicknesses of the AlN/PEI-TE layers are about 4 μm, 6 μm, and 8 μm, respectively, and the adjacent layers are tightly connected at interfaces without obvious defects, which is favorable for improving interfacial polarization and suppressing conduction loss. In addition, the NBBSCT-NN@A/PEI-specific element Na and the AlN/PEI-TE-specific element N are uniformly dispersed in the top and bottom layers, respectively (Fig. 3b, c), suggesting the successful fabrication of the bilayer-structured nanocomposites. Meanwhile, the bilayer nanocomposites still keep superior flexibility and high transmittance (Supplementary Fig. 18c). Supplementary Fig. 19a–c give Weibull distributions of the breakdown electric field and E_b, D-E loops, and capacitive characteristics of NBBSCT-NN@A/PEI-AlN/PEI-TE bilayer nanocomposites with various NBBSCT-NN@A/PEI and AlN/PEI-TE layer thicknesses. As shown, when the NBBSCT-NN@A/PEI thickness is thin, the bilayer nanocomposite exhibits a high E_b and slim D-E loops, but the D_{max} is low, leading to a small U_e. Conversely, when the NBBSCT-NN@A/PEI layer is thick, although the D_{max} can be enhanced, the E_b deteriorates, and the D-E loops become fat, resulting in a low η. Excitingly, when the thickness ratio of NBBSCT-NN@A/PEI to AlN/PEI-TE is optimized to 8:6, the bilayer nanocomposite achieves a balance of high D_{max}, low D_r, slim D-E loops, and high E_b, leading to both large U_e and high η. Consequently, this optimal configuration is selected for implementation in the present study. Temperature dependence of the ε_r and $\tan\delta$ of pristine PEI, and the

NBBSCT-NN@A/PEI and NBBSCT-NN@A/PEI-AlN/PEI-TE nanocomposites is shown in Fig. 3d. Compared to pristine PEI and NBBSCT-NN@A/PEI nanocomposites, the bilayer nanocomposites exhibit higher ε_r because of increased interfacial polarization (Fig. 3e and Supplementary Note 1), and lower $\tan\delta$. Also, the $\tan\delta$ of the bilayer nanocomposite at 25–150 °C is always smaller than 1.1%, and the ε_r varies slightly, i.e., from 4.05 to 3.92. Figure 3f presents Weibull distributions of the breakdown electric field and E_b of NBBSCT-NN@A/PEI-AlN/PEI-TE bilayer nanocomposites at various temperatures. The high β value indicates that excellent consistency in breakdown fields across temperatures, confirming superior film quality. As the temperature increases from 25 to 150 °C, the E_b value slightly decreases from 6577 kV cm^{-1} to 6341 kV cm^{-1}. Figure 3g and Supplementary Fig. 20 show D-E loops, D_{max}, D_r, and D_{max}-D_r of the bilayer nanocomposite at various temperatures. The D-E loops keep slim, the D_r is always smaller than 0.27 μC cm^{-2}, and the D_{max}-D_r is no less than 4.08 μC cm^{-2} during 25 to 150 °C. Thus, the U_e changes slightly from 13.78 J cm^{-3} to 12.35 J cm^{-3}, and the η is always higher than 90% at 25-150 °C, as observed in the inset of Fig. 3g, h. Figure 3i exhibits electric field dependence of the U_e and η for pristine PEI, and NBBSCT-NN@A/PEI and NBBSCT-NN@A/PEI-AlN/PEI-TE nanocomposites at 150 °C (date acquired from Supplementary Figs. 9, 21). As the electric field increases, the η of pristine PEI declines sharply, but encouragingly, the η of the NBBSCT-NN@A/PEI and NBBSCT-NN@A/PEI-AlN/PEI-TE decrease slightly. From pristine PEI to NBBSCT-NN@A/PEI and NBBSCT-NN@A/
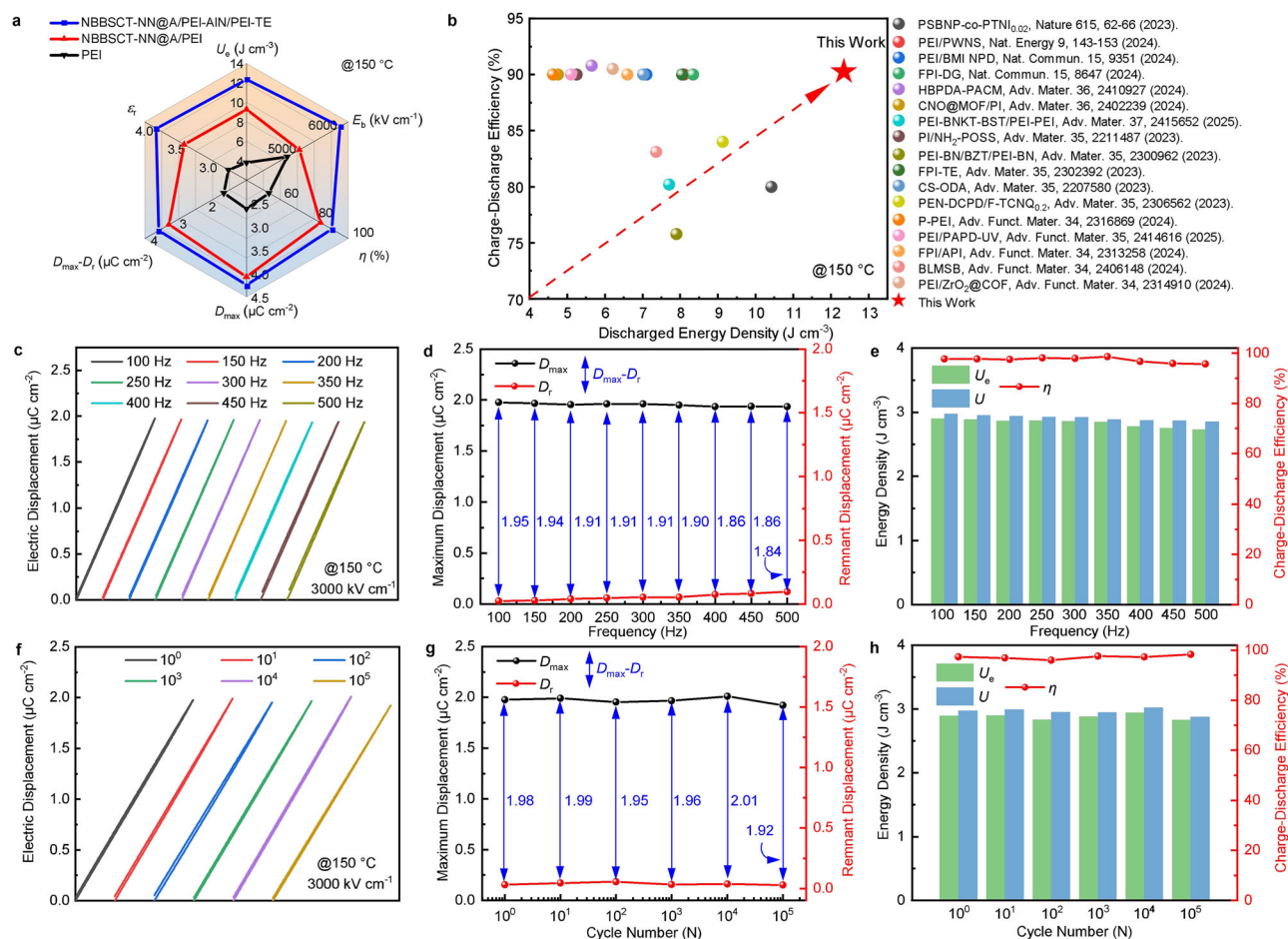
Fig. 4 | Comparison of capacitive performances, and frequency and cycle stability. a Capacitive parameters of pristine PEI, and NBBSCT-NN@A/PEI and NBBSCT-NN@A/PEI-AlN/PEI-TE nanocomposites at 150 °C. **b** Comparison of the U_e and η of this work and other reports at 150 °C. **c** Unipolar D-E loops, **d** D_{max}, D_r and D_{max}-D_r, and **e** U, U_e and η of the bilayer nanocomposites at 100-500 Hz, 3000 kV/cm and 150 °C. **f** Unipolar D-E loops, **g** D_{max}, D_r and D_{max}-D_r, and **h** U, U_e and η of the bilayer nanocomposites under different cycle numbers at 100 Hz, 3000 kV/cm and 150 °C.

PEI-AlN/PEI-TE, the U_e and η greatly improve from 3.79 J cm^{-3} to 9.29 J cm^{-3} and 12.35 J cm^{-3}, and from 53.17% to 83.58% and 90.25%, respectively.

Figure 4a gives overall capacitive performances of pristine PEI, and NBBSCT-NN@A/PEI and NBBSCT-NN@A/PEI-AlN/PEI-TE nanocomposites at 150 °C, demonstrating that introducing high-entropy ferroelectric nanofillers and designing bilayer structure are highly effective in achieving both large U_e and high η at elevated temperatures. Figure 4b compares U_e and η of the NBBSCT-NN@A/PEI-AlN/PEI-TE bilayer nanocomposite with those of state-of-the-art polymer and polymer composites reported at 150 °C [4,5,12,19,25–37]. Clearly, in previous studies, simultaneously achieving both large U_e and high η in one nanocomposite has been highly challenging. For instance, the PSBNP-co-PTNI$_{0.02}$ exhibits a large U_e of 10.42 J cm^{-3}, but the η is only 80%. On the other hand, the FPI-DG, FPI-TE, CS-ODA, etc., although achieve a high η of ≥90%, the U_e remains below 8.5 J cm^{-3}. By contrast, the NBBSCT-NN@A/PEI-AlN/PEI-TE bilayer nanocomposite exhibits a remarkable U_e of 12.35 J cm^{-3} and η of 90.25%, representing a significant breakthrough in advancing high-temperature polymer capacitors. Figure 4c-h give the frequency and cycling dependence of the capacitive performances for the bilayer nanocomposite at 150 °C and 3000 kV cm^{-1}. During 100–500 Hz and 1–10^5 cycle number, all D-E curves remain consistently slim and nearly coincident with only minor changes in D_r and D_{max}-D_r. Consequently, the variations of the U_e and η are merely respectively 6% and 2.5%, and 1.3% and 2.6% in the test frequency

and cycle range, meaning excellent frequency stability and an-fatigue characteristics of the capacitive properties.

In addition, for dielectric capacitors, superior actual charge-discharge capacity is critical for practical applications. Hence, discharge performances of pristine PEI, and NBBSCT-NN@A/PEI and NBBSCT-NN@A/PEI-AlN/PEI-TE nanocomposites at 150 °C and 2000 kV cm^{-1} are measured and characterized. Discharge current, energy density (U_d) and discharge rate, and power density (P_D) are presented in Supplementary Fig. 22a–c. The U_d can be given as follows[38]:

$$U_d = R \int I(t)^2 dt / V \qquad (3)$$

where V, I, and R represent the sample volume, discharge current, and load resistor, respectively. The discharge speed ($t_{0.9}$) is defined as the time required to release 90% of the U_d. For pristine PEI, the maximum discharge current, discharge speed and P_D ($P_D = U_d/t_{0.9}$) are 10.63 A, 19 ns, and 18.7 MW cm^{-3}. Encouragingly, these properties are significantly enhanced upon incorporating NBBSCT-NN@A nanoparticles, with further improvements achieved through the bilayer structure design. For instance, the maximum discharge current, discharge speed, and powder density of NBBSCT-NN@A/PEI nanocomposites, and NBBSCT-NN@A/PEI-AlN/PEI-TE bilayer nanocomposites are 12.69 A, 17 ns, and 28.17 MW cm^{-3}, and 15.49 A, 16 ns, and 31.71 MW cm^{-3}, respectively. Supplementary Fig. 22d compares

the P_D and $t_{0.9}$ of the NBBSCT-NN@A/PEI-AlN/PEI-TE bilayer nanocomposites obtained in this study with those of recently reported polymer and polymer nanocomposites at 150 °C[11,39–43]. As shown, the NBBSCT-NN@A/PEI-AlN/PEI-TE bilayer nanocomposites exhibit the fastest discharge speed and largest P_D among them, demonstrating their promising application potential in high temperature environment. In high-entropy materials, elements with varying atomic radii and valence states are randomly distributed at the A/B sites, leading to significant lattice distortions and oxygen octahedral tilts[44]. These structural features disrupt ferroelectric long-range order and promote the formation of polar nanoregions (PNRs), which significantly reduce polarization anisotropy and the domain switching barrier. As a result, when the applied electric field is removed, the induced ordered ferroelectric domains rapidly revert to a chaotic state, enabling an ultrafast discharge rate. The schematic diagram of the PNRs switching-induced short discharging time is given in the Supplementary Fig. 23. Thus, compared with pristine PEI, high-entropy ferroelectric NPs filled nanocomposites exhibit faster discharge rate. In addition, compared to the NBBSCT-NN@A/PEI nanocomposite, the NBBSCT-NN@A/PEI-AlN/PEI-TE bilayer nanocomposite achieves a further improvement in the discharge rate. Firstly, the introduction of AlN, due to its extremely low dielectric loss at high temperatures (<0.2% at ~230 °C)[45], effectively enhances the polarization response of the material, thereby increasing the discharge rate. Secondly, in the single-layer film, localized electric field concentration can lead to non-uniform polarization, causing polarization reversal delay. In contrast, the bilayer film optimizes the structure to achieve a more uniform electric field distribution, ensuring that dipole polarization can synchronously respond to changes in the electric field, further enhancing the dynamic response rate of the dielectric material.

Underlying mechanism of improved high-temperature energy storage properties in NBBSCT-NN@A/PEI and NBBSCT-NN@A/PEI-AlN/PEI-TE nanocomposites

To explore the underlying mechanism of enhanced high-temperature capacitive properties in NBBSCT-NN@A/PEI and NBBSCT-NN@A/PEI-AlN/PEI-TE nanocomposites, the leakage current and resistivity variations of pristine PEI, and NBBSCT-NN@A/PEI and NBBSCT-NN@A/PEI-AlN/PEI-TE nanocomposites under different electric fields and temperatures are studied (Supplementary Figs. 24, 25). For pristine PEI, as the temperature increases from 25 to 150 °C, the leakage current rises significantly while the resistivity drops sharply. Notably, introducing NBBSCT-NN@A into the nanocomposites effectively suppresses leakage current at high electric fields and elevated temperatures, with further reduction achieved by constructing bilayer structure. Figure 5a-c presents contour plots of leakage current density for pristine PEI, and NBBSCT-NN@A/PEI and NBBSCT-NN@A/PEI-AlN/PEI-TE nanocomposites under varying temperatures and electric fields, offering a clear visualization of their combined effects. The lower leakage current density in the nanocomposites than that in pristine PEI help enhance high-temperature energy storage capacity by minimizing conduction loss. The hopping distances (λ) of charge carriers, calculated by the hopping conduction model (Supplementary Note 2), reduce from 2.44 nm of pristine PEI to 1.72 nm of NBBSCT-NN@A/PEI nanocomposites, and 1.18 nm of NBBSCT-NN@A/PEI-AlN/PEI-TE bilayer nanocomposites (Fig. 5d), indicating increased charge trap depth[28,31]. This trend is further supported by thermally stimulated depolarization currents (TSDC) measurements. As shown in Fig. 5e, the TSDC curves of pristine PEI, and NBBSCT-NN@A/PEI, and NBBSCT-NN@A/PEI-AlN/PEI-TE nanocomposites exhibit distinct current peaks, which are related to space charge polarization of trapped carriers in deep traps[8,10]. The upward shift and enhanced intensity of these peaks from pristine PEI to NBBSCT-NN@A/PEI, and NBBSCT-NN@A/PEI-AlN/PEI-TE demonstrates that deeper charge traps and more trap sites for

charge carriers are formed in NBBSCT-NN@A/PEI and NBBSCT-NN@A/PEI-AlN/PEI-TE nanocomposites, thereby suppressing conduction loss and resulting in larger E_b, U_e, and η[8,10]. To understand increased trap depth in NBBSCT-NN@A/PEI nanocomposites, the band diagram at the interfaces of NBBSCT-NN@A and PEI is plotted in the inset of Fig. 5e. The E_g and electron affinity (E_a), and work function (ϕ_A) of PEI and Al_2O_3 are 3.1 eV and 8.6 eV, 2.99 eV and 2.0 eV, and 4.43 eV and 3.76 eV, respectively[11,46]. Large differences between the E_c energy levels of Al_2O_3 and the LUMO energy levels of PEI, as well as between the E_v energy levels of Al_2O_3 and HOMO energy levels of PEI create deep charge carrier traps at the Al_2O_3/PEI interfaces, which effectively explains suppressed leakage current in NBBSCT-NN@A/PEI nanocomposites compared to pristine PEI. Additionally, interfacial polarization leads to an accumulation of negative charges at the NBBSCT-NN@A/PEI and AlN/PEI-TE interfaces (Fig. 3e and Supplementary Note 1), further restricting electron transport and reducing leakage current in the bilayer nanocomposites. The mechanical properties of the polymers and nanocomposites are also investigated. Figure 5f presents the Young's modulus (Y) of pristine PEI, NBBSCT-NN@A/PEI and NBBSCT-NN@A/PEI-AlN/PEI-TE nanocomposites. The Y values of NBBSCT-NN@A/PEI and NBBSCT-NN@A/PEI-AlN/PEI-TE nanocomposites are 1.85 and 2.9 GPa, respectively, being significantly higher than 0.87 GPa of pristine PEI, which can greatly inhibit the electromechanical breakdown and enhance the E_b. To further investigate the influences of incorporating NBBSCT-NN@A high-entropy NPs and designing bilayer structure on high-temperature capacitive performances of polymer nanocomposites, we simulate internal temperature distributions of pristine PEI, and NBBSCT-NN@A/PEI and NBBSCT-NN@A/PEI-AlN/PEI-TE nanocomposites at the ambient temperature of 150 °C and the electric field of 2500 kV cm⁻¹ by COMSOL Multiphysics (Fig. 5g-i). The internal temperatures of NBBSCT-NN@A/PEI and NBBSCT-NN@A/PEI-AlN/PEI-TE nanocomposites are 175 °C and 152 °C, respectively, which are significantly lower than that (272 °C) of pristine PEI. This is due to pronounced reduction in leakage current density and marked enhancement in thermal conductivity, that is, from 0.23 W m⁻¹ K⁻¹ for pristine PEI to 0.37 W m⁻¹ K⁻¹ for NBBSCT-NN@A/PEI and 0.47 W m⁻¹ K⁻¹ for NBBSCT-NN@A/PEI-AlN/PEI-TE. The generated Joule heat in pristine PEI deteriorates not only high-temperature capacitive performances, but also the device reliability and service lifetime.

Finite element simulations of real-time electric field and electric potential distributions with electrical tree evolving

To better understand breakdown process, we simulate the real-time distributions of the electric field and electric potential with electrical tree evolving in pristine PEI, and NBBSCT-NN@A/PEI and NBBSCT-NN@A/PEI-AlN/PEI-TE nanocomposites using MATLAB and COMSOL Multiphysics (Supplementary Note 3). The ε_r of the NBBSCT-NN, Al_2O_3, AlN, PEI, and PEI-TE are set to 1635, 9.5, 9.8, 3, and 2.8 (Supplementary Fig. 26), respectively[9,24]. As shown in Fig. 6 and Supplementary Fig. 27, the differences in ε_r between NBBSCT-NN, Al_2O_3, AlN, PEI, and PEI-TE cause redistribution of the electric potential and applied electric field in the nanocomposites.

In pristine PEI, electrical trees propagate throughout the entire material, leading to complete breakdown. However, when the core-shell structured NBBSCT-NN@A NPs are introduced into the PEI matrix, they impede electrical tree evolution. This results in increased branching of electrical trees and energy dissipation during propagation, gradually reducing the electric potential difference near the tree tips. Consequently, electrical tree growth is hindered before reaching the top boundary, improving the E_b. In the NBBSCT-NN@A/PEI-AlN/PEI-TE bilayer nanocomposites, electrical tree propagation is further blocked at the interfacial regions between adjacent layers due to ε_r differences between PEI and PEI-TE, leading to even higher E_b. In summary, these theoretical simulations corroborate the experimental measurements, demonstrating how material
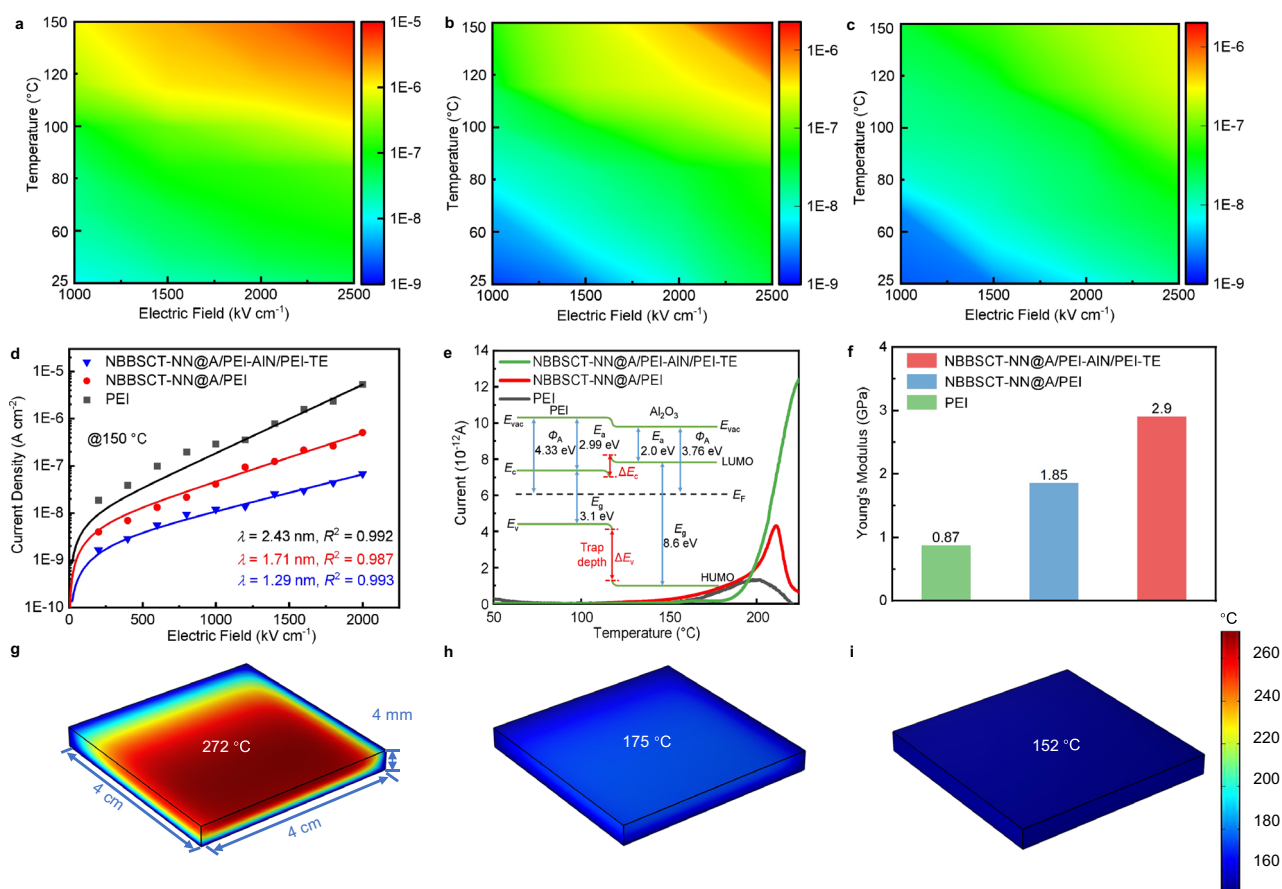
Fig. 5 | Underlying mechanism of enhanced high-temperature dielectric energy storage properties. Contour plots of the leakage current density of (**a**) pristine PEI, **b** NBBSCT-NN@A/PEI nanocomposites, and **c** NBBSCT-NN@A/PEI-AlN/PEI-TE bilayer nanocomposites. **d** Leakage current density and hopping distance of charge carriers (R^2 being the goodness of fitting) at 150 °C, and **e** TSDC spectra in pristine PEI, and NBBSCT-NN@A/PEI and NBBSCT-NN@A/PEI-AlN/PEI-TE nanocomposites. The inset gives the band diagram at the NBBSCT-NN@A/PEI interfaces. E_{vac} is the vacuum energy level, and E_F is the Fermi energy level. E_c and E_v are the conduction band and valence band, respectively. LUMO and HOMO are the lowest unoccupied molecular orbital and highest occupied molecular orbital of the PEI, respectively. **f** Young's modulus in pristine PEI, and NBBSCT-NN@A/PEI and NBBSCT-NN@A/PEI-AlN/PEI-TE nanocomposites. Simulated steady-state temperature distribution in (**g**) pristine PEI, **h** NBBSCT-NN@A/PEI nanocomposites, and **i** NBBSCT-NN@A/PEI-AlN/PEI-TE bilayer nanocomposites under an electric field of 2500 kV cm^{-1} and the ambient temperature of 150 °C.

design influences electrical tree suppression and enhances breakdown resistance.

In summary, NBBSCT-NN@A high-entropy ferroelectric NPs/ PEI nanocomposites, and NBBSCT-NN@A/PEI-AlN/PEI-TE bilayer nanocomposites are designed and developed. Due to high ε_r and large D_{max} of NBBSCT-NN high-entropy ferroelectric fillers and interfacial polarization effect, these nanocomposites exhibit significantly enhanced ε_r and increased D_{max} compared to pristine PEI. Moreover, they demonstrate suppressed hysteresis and conduction loss, and remarkably improved E_b at high temperatures. For instance, at 150 °C, the E_b improves from 5035 kV cm^{-1} for pristine PEI to 5291 kV cm^{-1} for NBBSCT-NN@A/PEI nanocomposites, and further to 6341 kV cm^{-1} for NBBSCT-NN@A/PEI-AlN/PEI-TE bilayer nanocomposites. Benefiting from high E_b, ε_r, and D_{max}-D_r, the bilayer nanocomposites exhibit an ultrahigh U_e of 12.35 J cm^{-3} at 150 °C and 6341 kV cm^{-1}, surpassing existing dielectric polymers and polymer composites, along with an ultrahigh η of 90.25%. Encouragingly, they also possess excellent actual discharge capacity with an ultrahigh power density of 31.7 MW cm^{-3} and an ultrafast discharge rate of 16 ns at 2000 kV cm^{-1}. This work provides a groundbreaking strategy for designing high-performance dielectric capacitors capable of reliable operation in extreme environments.

Methods
Preparation of NBBSCT-NN@A NPs
0.8(Na$_{0.2}$Bi$_{0.2}$Ba$_{0.2}$Sr$_{0.2}$Ca$_{0.2}$)TiO$_3$-0.2NaNbO$_3$ powders were obtained using solid-state reaction way. Na$_2$CO$_3$、Bi$_2$O$_3$、BaCO$_3$、SrCO$_3$、 CaCO$_3$、TiO$_2$、and Nb$_2$O$_5$ with purities higher than 99% were as raw materials and weighted according to the above formula. Then, they were mixed, milled for 12 h, and calcined at 850 °C for 2 h with the goal of fabricating NBBSCT-NN powders. To obtain NBBSCT-NN@Al$_2$O$_3$ particles, aluminum isopropoxide (C$_9$H$_{21}$AlO$_3$, 99.8%) was dissolved in ethylene glycol ether (C$_4$H$_{10}$O$_2$, 99%) under stirring at 60 °C for 30 min and subsequently, acetylacetone (C$_5$H$_8$O$_2$, 99.7%) was added, and stirring continued for another 30 min. After that, acetic acid (CH$_3$COOH, 99.9%) was introduced and the mixture was stirred at 90 °C for 30 min to form a stable Al$_2$O$_3$ sol. In the following, the NBBSCT-NN powders were mixed with Al$_2$O$_3$ sol in different ratios, and then grinded, dried, and calcined at 600 °C for 2 h. To characterize electrical performances of NBBSCT-NN and NBBSCT-NN@A ceramics, NBBSCT-NN and NBBSCT-NN@A powders were pressed into discs and sintered at 1140 °C for 2 h in air.

Fabrication of the nanocomposites
To prepare NBBSCT-NN@A/PEI nanocomposites, PEI particles were first dispersed in the N-methylpyrrolidone (NMP) solvent, and stirred
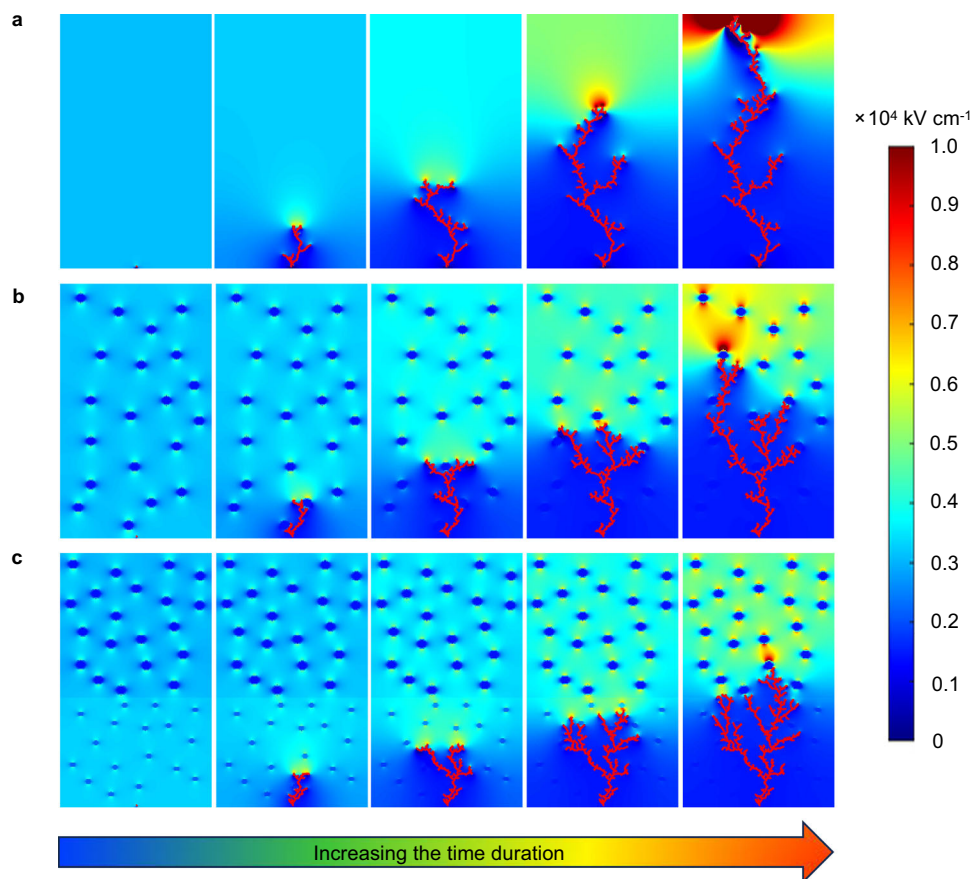
Fig. 6 | Finite element simulations. Simulated real-time evolution of electric field distributions with electrical trees (breakdown paths) propagation in (**a**) pristine PEI, **b** NBBSCT-NN@A/PEI nanocomposites, and **c** NBBSCT-NN@A/PEI-AlN/PEI-TE bilayer nanocomposites.

at 75 °C for 3 h. Meanwhile, the NBBSCT-NN@A NPs were also dispersed in NMP solvent via ultrasonically stirring at room temperatures. After that, the two solutions were mixed and then stirred magnetically for 12 h. The resulting mixture was cast onto a clean glass substrate, and dried in a vacuum oven at 50 °C for 12 h to evaporate the NMP solvent, followed by heating at 160 °C for 10 min to remove residual solvent. In order to fabricate NBBSCT-NN@A/PEI-AlN/PEI-TE bilayer nanocomposites, the uniformly dispersed AlN/PEI-TE precursor solution was cast onto the pre-formed NBBSCT-NN@A/PEI films before heating. The films were dried at 50 °C for 12 h and then subjected to a final drying step at 220 °C for 10 min. Finally, the nanocomposites were peeled off the glass substrate. Schematic illustration of the preparation process for NBBSCT-NN@A/PEI and NBBSCT-NN@A/PEI-AlN/PEI-TE nanocomposites was provided in Supplementary Figs. 28, 29, respectively. To measure electrical properties, Au electrodes with a 2 mm diameter were deposited onto polymer nanocomposites.

Characterization
The microstructure and elemental mapping images of NBBSCT-NN@A NPs were achieved using the Talos F200X transmission electron microscopy (TEM, FEI, USA). The compositions were examined by the ESCALAB 250Xi X-ray photoelectron spectroscopy (XPS, Thermo Fisher Scientific, USA). The crystal structure was analyzed by the D8 Advance X-ray diffraction (XRD, Bruker, Germany). The surface, cross-section, and elemental mapping images of the nanocomposites were measured by the SIGMA 500 field-emission scanning electron microscopy (FE-SEM, Zeiss, Germany). The Fourier transform infrared (FTIR) spectrum was recorded with the Nicolet iS50 FTIR spectrometer (Thermo Fisher Scientific, USA). Dielectric properties were acquired by

the HP4294A precision impedance analyzer (Agilent, USA). The thermally stimulated depolarization current was measured by the PCTS-2500 pyroelectric test system (Wuhan Yanhe Technology, China). Young's modulus of pristine PEI and NBBSCT-NN@A/PEI nanocomposites, and NBBSCT-NN@A/PEI-AlN/PEI-TE bilayer nanocomposites are measured by the iNano nanoindenter (KLA-Tencor, USA) and the 68TM-10 universal tensile testing machine (Instron, USA), respectively. The thermal conductivity is calculated based on the specific heat, thermal diffusivity, and density of the samples. The specific heat capacity was recorded using the differential scanning calorimetry (DSC2500, TA, USA). The thermal diffusivity was measured by the LFA 467 HyperFlash system (NETZSCH, Germany). The E_b was evaluated by the withstand voltage tester (NJC5010, Tongguo Technology, China). D-E loops and leakage current were characterized using the Precision LC II ferroelectric measurement equipment (Radiant, USA). Charge-discharge properties were evaluated via a discharge resistance, inductance, and capacitance (RLC) load circuit (CFD-003, Tongguo Technology, China).

Data availability
All data supporting this study and its findings are available within the article and its Supplementary Information. The data corresponding to this study are available from the corresponding authors upon request.

References
1. Yang, M. et al. Polymer nanocomposite dielectrics for capacitive energy storage. *Nat. Nanotechnol.* **19**, 588–603 (2024).
2. Feng, Q.-K. et al. Recent progress and future prospects on all-organic polymer dielectrics for energy storage capacitors. *Chem. Rev.* **122**, 3820–3878 (2022).

3. Liu, J. et al. Ferroelectric tungsten bronze-based ceramics with high-energy storage performance via weakly coupled relaxor design and grain boundary optimization. *Nat. Commun.* **15**, 8651 (2024).

4. Chen, J. et al. Ladderphane copolymers for high-temperature capacitive energy storage. *Nature* **615**, 62–66 (2023).

5. Zhang, Q. et al. Scalable all polymer dielectrics with self-assembled nanoscale multiboundary exhibiting superior high temperature capacitive performance. *Nat. Commun.* **15**, 9351 (2024).

6. Li, H. et al. Dielectric polymers for high-temperature capacitive energy storage. *Chem. Soc. Rev.* **50**, 6369–6400 (2021).

7. Li, Q. et al. Flexible high-temperature dielectric materials from polymer nanocomposites. *Nature* **523**, 576–579 (2015).

8. Ai, D. et al. Tuning nanofillers in in situ prepared polyimide nanocomposites for high-temperature capacitive energy storage. *Adv. Energy Mater.* **10**, 1903881 (2020).

9. Zha, J.-W. et al. Polymer dielectrics for high-temperature energy storage: constructing carrier traps. *Prog. Mater. Sci.* **140**, 101208 (2023).

10. Ren, L. et al. High-temperature high-energy-density dielectric polymer nanocomposites utilizing inorganic core-shell nanostructured nanofillers. *Adv. Energy Mater.* **11**, 2101297 (2021).

11. Dong, J. et al. A facile in situ surface-functionalization approach to scalable laminated high-temperature polymer dielectrics with ultrahigh capacitive performance. *Adv. Funct. Mater.* **31**, 2102644 (2021).

12. Yang, M. et al. Roll-to-roll fabricated polymer composites filled with subnanosheets exhibiting high energy density and cyclic stability at 200°C. *Nat. Energy* **9**, 143–153 (2024).

13. Li, J. et al. Enhanced dielectric performance with high-temperature stability by interface-modulation of the core-shell structured imide-polymer@BT nanohybrids in PEI-based nanocomposites. *J. Mater. Chem. C* **11**, 7289–7298 (2023).

14. Zhu, C. et al. Grain size engineered high-performance nanograined $BaTiO_3$-based ceramics: experimental and numerical prediction. *J. Am. Ceram. Soc.* **104**, 273–283 (2021).

15. Zhang, M. et al. Ultrahigh energy storage in high-entropy ceramic capacitors with polymorphic relaxor phase. *Science* **384**, 185–189 (2024).

16. Gao, Y. et al. Optimizing high-temperature energy storage in tungsten bronze-structured ceramics via high-entropy strategy and bandgap engineering. *Nat. Commun.* **15**, 5869 (2024).

17. Chen, L. et al. Giant energy-storage density with ultrahigh efficiency in lead-free relaxors via high-entropy design. *Nat. Commun.* **13**, 3089 (2022).

18. Hostaša, J. et al. Thermal conductivity of Al_2O_3-ZrO_2 composite ceramics. *J. Am. Ceram. Soc.* **94**, 4404–4409 (2011).

19. Yang, M. et al. Polyimides physically crosslinked by aromatic molecules exhibit ultrahigh energy density at 200 °C. *Adv. Mater.* **35**, 2302392 (2023).

20. Yang, S. et al. Simultaneously enhanced thermal conductivity and dielectric properties of borosilicate glass-based LTCC with AlN and h-BN additions. *J. Eur. Ceram. Soc.* **43**, 4814–4825 (2023).

21. Dong, X. et al. Versatile landscape of low-*k* polyimide: theories, synthesis, synergistic properties, and industrial integration. *Chem. Rev.* **124**, 7674–7711 (2024).

22. Li, J. et al. Grain-orientation-engineered multilayer ceramic capacitors for energy storage applications. *Nat. Mater.* **19**, 999–1005 (2020).

23. Li, X. et al. High-temperature capacitive energy storage in polymer nanocomposites through nanoconfinement. *Nat. Commun.* **15**, 6655 (2024).

24. Tsao, J. et al. Ultrawide-bandgap semiconductors: research opportunities and challenges. *Adv. Electron. Mater.* **4**, 1600501 (2018).

25. Yang, M. et al. Enhanced high-temperature energy storage performances in polymer dielectrics by synergistically optimizing bandgap and polarization of dipolar glass. *Nat. Commun.* **15**, 8647 (2024).

26. Huang, W. et al. Alicyclic polyimide with multiple breakdown self-healing based on gas-condensation phase validation for high temperature capacitive energy storage. *Adv. Mater.* **36**, 2410927 (2024).

27. Liu, X. et al. Atomic-level matching metal-ion organic hybrid interface to enhance energy storage of polymer-based composite dielectrics. *Adv. Mater.* **36**, 2402239 (2024).

28. Guo, Y. et al. Ultra-high capacitive energy storage density at 150 °C achieved in polyetherimide composite films by filler and structure design. *Adv. Mater.* **37**, 2415652 (2025).

29. Dong, J. et al. Scalable polyimide-organosilicate hybrid films for high-temperature capacitive energy storage. *Adv. Mater.* **35**, 2211487 (2023).

30. Liu, H. et al. Single-crystalline $BaZr_{0.2}Ti_{0.8}O_3$ membranes enabled high energy density in PEI-based composites for high-temperature electrostatic capacitors. *Adv. Mater.* **35**, 2300962 (2023).

31. Pan, Z. et al. Tailoring poly(Styrene-*co*-maleic anhydride) networks for all-polymer dielectrics exhibiting ultrahigh energy density and charge-discharge efficiency at elevated temperatures. *Adv. Mater.* **35**, 2207580 (2023).

32. Chen, J. et al. Aromatic-free polymers based all-organic dielectrics with breakdown self-healing for high-temperature capacitive energy storage. *Adv. Mater.* **35**, 2306562 (2023).

33. Pei, J. et al. Flexible high-temperature polymer dielectrics induced by ultraviolet radiation for high efficient energy storage. *Adv. Funct. Mater.* **34**, 2316869 (2024).

34. Wang, Q. et al. Roll-to-roll production of high-performance all-organic polymer nanocomposites for high-temperature capacitive energy storage. *Adv. Funct. Mater.* **35**, 2414616 (2025).

35. Liu, M. et al. Significant enhancement in dielectric properties of polyimide alloys through a two-phase interlocking structure. *Adv. Funct. Mater.* **34**, 2313258 (2024).

36. Dang, Z. et al. Ultrahigh dielectric energy density and efficiency in PEI-based gradient layered polymer nanocomposite. *Adv. Funct. Mater.* **34**, 2406148 (2024).

37. Xie, Z. et al. Interfacial engineering using covalent organic frameworks in polymer composites for high-temperature electrostatic energy storage. *Adv. Funct. Mater.* **34**, 2314910 (2024).

38. Fan, Z. et al. Superior energy storage capacity of polymer-based bilayer composites by introducing 2D ferroelectric micro-sheets. *Nat. Commun.* **16**, 1180 (2025).

39. Dong, J. et al. Enhancing high-temperature capacitor performance of polymer nanocomposites by adjusting the energy level structure in the micro-/meso-scopic interface region. *Nano Energy* **99**, 107314 (2022).

40. Shang, Y. et al. Achieving synergistic improvement in dielectric and energy storage properties at high-temperature of all-organic composites *via* physical electrostatic effect. *Mater. Horiz.* **11**, 1528–1538 (2024).

41. Li, S. et al. Enhanced high-temperature energy storage properties of polymer composites by interlayered metal nanodots. *J. Mater. Chem. A* **10**, 18773–18781 (2022).

42. Li, L. et al. Wide-bandgap fluorides/polyimide composites with enhanced energy storage properties at high temperatures. *Chem. Eng. J.* **435**, 135059 (2022).

43. Sun, H. et al. Significantly enhanced high-temperature energy storage performance for polymer composite films with gradient distribution of organic fillers. *Chem. Eng. J.* **497**, 154546 (2024).

44. Wei, T. et al. High-entropy assisted capacitive energy storage in relaxor ferroelectrics by chemical High-entropy assisted capacitive energy storage in relaxor ferroelectrics by chemical short-range order. *Nat. Commun.* **16**, 807 (2025).

45. Wang, K. et al. Aluminum-vacancy-related dielectric relaxations in AlN ceramics. *J. Am. Ceram. Soc.* **101**, 2009–2016 (2018).
46. Zhang, T. et al. Polymer dielectric films exhibiting superior high-temperature capacitive performance by utilizing an inorganic insulation interlayer. *Mater. Horiz.* **9**, 1273–1282 (2022).

Author contributions

X. Zhao, L. Zhang, and Q.F. Zhang. designed the experiments. X. Zhao, L. Zhang, Z.H. Fan, Y.Y. H. carried out the experiments and performed the simulation. X. Zhao., L. Zhang., Y.M. Hu., Y.B. He., D.W. Wang., and Q.F. Zhang. analyzed the data. X. Zhao drafted the manuscript. Y.M. Hu., M. Shen., Z. Wang., Y.B. He., D.W. Wang., and Q.F. Zhang revised the manuscript. All authors discussed the results on the manuscript.

Competing interests

The authors declare no competing interests.

Additional information

Supplementary information The online version contains supplementary material available at https://doi.org/10.1038/s41467-025-60683-8.

Correspondence and requests for materials should be addressed to Yongming Hu, Yunbin He, Dawei Wang or Qingfeng Zhang.

Peer review information *Nature Communications* thanks Ch. Thirmal, Srinibas Satapathy, and the other anonymous reviewer(s) for their contribution to the peer review of this work. A peer review file is available.

Reprints and permissions information is available at http://www.nature.com/reprints

Publisher's note Springer Nature remains neutral with regard to jurisdictional claims in published maps and institutional affiliations.